United Kingdom Atomic Energy Authority

UKAEA FUS 530

P.M. Derlet, S.L. Dudarev

Million-atom molecular dynamics simulations of magnetic iron

Million-atom molecular dynamics simulations of magnetic iron

P.M. Derlet, S.L. Dudarev

EURATOM/UKAEA Fusion Association, Culham Science Centre, OX14 3DB, Abingdon, UK

UKAEA FUS 530

EURATOM/UKAEA Fusion

Million-atom molecular dynamics simulations of magnetic iron

P.M. Derlet, S.L. Dudarev

July 2006

EURATOM/UKAEA Fusion Association

Culham Science Centre
Abingdon
Oxfordshire
OX14 3DB
United Kingdom

Telephone: +44 1235 466586
Facsimile: +44 1235 466435

Million-atom molecular dynamics simulations of magnetic iron.

P. M. Derlet[a] and S. L. Dudarev[b]

[a] *Paul Scherrer Institute, CH-5232 Villigen PSI, Switzerland*

[b] *EURATOM/UKAEA Fusion Association,*

Culham Science Centre, Oxfordshire OX14 3DB, UK[*]

(Dated: July 12, 2006)

Abstract

The problem of large-scale molecular dynamics simulations of iron has recently attracted attention in connection with the need to understand the microscopic picture of radiation damage in ferritic steels. In this paper we review the development of a new interatomic potential for magnetic iron, and describe the first large-scale atomistic simulations performed using the new method. We investigate the structure and thermally activated mobility of self-interstitial atom clusters and show that the spatial distribution of magnetic moments around a cluster is well correlated with the distribution of hydrostatic pressure, highlighting the significant part played by magneto-elasticity in the treatment of radiation damage. We show that self-interstitial atom clusters exhibit a transition from relatively immobile configurations containing $\langle 110 \rangle$-like groups of atoms to $\langle 111 \rangle$-like configurations occurring at a critical cluster size $N_c \sim 5$ atoms. We discuss implications of this finding for the treatment of cascade damage effects, and the possibility of observing new low-temperature resistivity recovery stages in neutron-irradiated α-iron.

PACS numbers:

[*]Electronic address: Peter.Derlet@psi.ch,Sergei.Dudarev@UKAEA.org.uk

I. INTRODUCTION

From the early work by Wigner [1], and by Gell-Mann and Brueckner [2], it has been known that in the low density limit the behaviour of an electron gas is dominated by the exchange and correlation effects. Electron correlation effects also dominate the properties and structure of narrow-band materials where the kinetic energy of electrons (proportional to the bandwidth) is comparable with the energy of the on-site Hubbard repulsion between electrons [3]. Since the *effective* width of the band $\mathcal{W}$ is inversely proportional to the density of states at the Fermi energy, $\mathcal{W} \sim 1/D(\epsilon_F)$, exchange and correlation effects play a particularly important part in the case of body-centred cubic (bcc) iron where $D(\epsilon_F)$ is large, giving rise to the onset of ferromagnetism [4].

The presence of magnetism has important implications for the structural stability of materials. Indeed, atomic configurations depend sensitively on magnetic ordering in the case where the magnetic energy and the difference between energies of competing crystal structures are of the same order of magnitude. This was first highlighted in a pioneering work by Hasegawa and Pettifor [5] where they showed that the presence of magnetism stabilizes the bcc α-phase of iron. Furthermore, Hasegawa and Pettifor found that the entropy term associated with magnetic fluctuations in the face-centred cubic (fcc) phase was responsible for the phase transition from the bcc α to the fcc γ phase occurring at approximately 912°C. A series of most unusual magnetic and structural transformations in iron resulting from the interplay between the kinetic energy effects associated with electron hopping, and the electron correlations effects responsible for magnetism, are described in a recent review by Pettifor [6].

Ferromagnetism in iron can be treated using the phenomenological band model proposed by Stoner [7]. This model was developed and applied to a variety of metallic systems by Wohlfarth [8], Edwards and Wohlfarth [9], and by Pettifor [10]. However, so far the analysis of the relationship between the structural and magnetic properties was focused mainly on the treatment of spatially homogeneous crystalline solids. It excluded the treatment of strong localised deformations, for example point defects, dislocations and grain boundaries. The development of a good understanding of magnetic properties of dislocations and other defects is essential for modelling mechanical properties of magnetic materials, as well as for modelling microstructural evolution of iron-based alloys and steels under irradiation. For example, in

a recent comprehensive review of the currently available modelling methodologies [11] it was noted that '...the absence of a physically sensible treatment of magnetization points to more fundamental problems in the many-body potential concept.' The need to develop a local representation of magnetic effects consistent with the treatment of interatomic forces comes from the fact that it is only a local model that is able to describe an interstitial atom defect or an edge dislocation, where the level of local deformation approaches $\sim 15\%$ [12]. The fact that the pattern of ordering of relative energies of formation of basic interstitial atom defects in all the non-magnetic body-centred cubic (bcc) metals is different from that of ferromagnetic bcc iron [13] illustrates the effect of magnetism on forces acting between atoms. The significant part played by itinerant ferromagnetism in intergranular cohesion in iron was highlighted by Yeşilleten *et al.* [14], where the increase in magnetic moments in a grain boundary was found to stabilize its structure. Nanocrystalline iron is another example where interplay between the topology of local structure of grain boundaries and magnetism has a strong effect on the conductivity of the material [15].

In this paper we go beyond previous non-magnetic empirical models for iron such as in [16] and review a newly developed approach [17] to molecular dynamics simulations of magnetic iron that is different to that recently suggested in Ref. [18]. The approach is based on a combination of the Stoner model of ferromagnetism and the Ginzburg-Landau model. The latter represents the simplest known model of a magnetic phase transition and provides a convenient means for evaluating the energies of the high- and low-symmetry magnetic solutions [19]. By combining the Stoner and the Ginzburg-Landau models we are able to find a suitable functional representation for the magnetic part of the many-body interatomic potential. In this paper we focus primarily on applications of the new method to fast large-scale molecular dynamics simulations investigating, for example, magneto-elastic fields associated with radiation-induced defects and dislocation loops. We also study the dynamics of radiation-induced defects in iron and show that at low temperatures self-interstitial atom clusters containing fewer than five atoms form immobile $\langle 110 \rangle$-like configurations. On the other hand, larger clusters adopt $\langle 111 \rangle$-like configurations and perform one-dimensional Brownian motion. The onset of low-temperature mobility occurring at a certain critical size of a self-interstitial atom cluster predicted in our simulations may be observed experimentally in the form of new low-temperature resistivity recovery stages present in neutron-irradiated but absent in electron-irradiated iron.

II. THE STONER INSTABILITY AND THE ONSET OF FERROMAGNETISM

In the Stoner model the total band energy per atom is given by the sum of energies of all the occupied spin-up and spin-down electronic states minus a term describing the two-body correlations between electrons [4]

$$E_{tot} = E_\uparrow + E_\downarrow - I\zeta^2/4, \tag{1}$$

where $E_\uparrow$ and $E_\downarrow$ are the energies of spin up and spin down sub-bands, $\zeta = N_\uparrow - N_\downarrow$ is the magnetic moment of an atom, and I is the Stoner parameter.

The energies $E_\uparrow$ and $E_\downarrow$ of the majority and minority spin sub-bands are given by the integrals of the projected on-site density of states up to the Fermi energies $\epsilon_{F\uparrow}$ and $\epsilon_{F\downarrow}$ of spin up and spin down electrons [4, 20, 21],

$$E_\uparrow = \int_{-\infty}^{\epsilon_{F\uparrow}} ED(E)dE, \quad E_\downarrow = \int_{-\infty}^{\epsilon_{F\downarrow}} ED(E)dE. \tag{2}$$

Similarly, the band occupation numbers are

$$N_\uparrow = \int_{-\infty}^{\epsilon_{F\uparrow}} D(E)dE, \quad N_\downarrow = \int_{-\infty}^{\epsilon_{F\downarrow}} D(E)dE. \tag{3}$$

and hence the total number of electrons per atom, which in a metal is constant because of the local charge neutrality condition [22], is given by

$$N = \int_{-\infty}^{\epsilon_{F\uparrow}} D(E)dE + \int_{-\infty}^{\epsilon_{F\downarrow}} D(E)dE = const. \tag{4}$$

In principle, the expression for the total energy given by equation (1) can also be obtained starting from energies of effective single particle states. However the fact that the problem of magnetism requires taking into account the Stoner term describing interaction between electrons makes the single-particle representation incomplete. Hence the expression for the total energy evaluated using a single-particle model must also contain the so-called double counting correction (see Appendix for more detail). This double counting term accounts for the difference between the exact energy of a system of interacting electrons and the sum of effective single particle energies of occupied states. The fact that the two are not equal reflects the two-particle nature of the problem of magnetism.

The magnetic moment ζ is given by the difference between the occupation numbers of spin up and spin down states

$$\zeta = \int_{-\infty}^{\epsilon_{F\uparrow}} D(E)dE - \int_{-\infty}^{\epsilon_{F\downarrow}} D(E)dE = \int_{\epsilon_{F\downarrow}}^{\epsilon_{F\uparrow}} D(E)dE. \tag{5}$$

A simple calculation involving equations (1), (4) and (5) shows that in the limit $\zeta \ll 1$ the total energy is quadratic in ζ, namely

$$E_{tot}(\zeta) = E_{tot}(0) + \left[\frac{1}{D\left(\epsilon_F\right)} - I\right]\frac{\zeta^2}{4} + ... \tag{6}$$

where ϵ_F is the Fermi energy of the non-magnetic state. In the case where $D(\epsilon_F)I > 1$ the non-magnetic state of the material is no longer stable with respect to the onset of ferromagnetism. The equilibrium value of the magnetic moment is determined by the condition $\partial E/\partial\zeta = 0$. Using this condition and treating N and ζ as independent variables, from equations (1)-(5) we find that at equilibrium

$$\begin{aligned} \epsilon_{F\uparrow}D(\epsilon_{F\uparrow})\frac{\partial\epsilon_{F\uparrow}}{\partial\zeta} + \epsilon_{F\downarrow}D(\epsilon_{F\downarrow})\frac{\partial\epsilon_{F\downarrow}}{\partial\zeta} - \frac{1}{2}I\zeta &= 0 \\ D(\epsilon_{F\uparrow})\frac{\partial\epsilon_{F\uparrow}}{\partial\zeta} + D(\epsilon_{F\downarrow})\frac{\partial\epsilon_{F\downarrow}}{\partial\zeta} &= 0 \\ D(\epsilon_{F\uparrow})\frac{\partial\epsilon_{F\uparrow}}{\partial\zeta} - D(\epsilon_{F\downarrow})\frac{\partial\epsilon_{F\downarrow}}{\partial\zeta} &= 1. \end{aligned} \tag{7}$$

By combining these equations we arrive at the condition of equilibrium [21, 23]

$$I\zeta = I\int_{\epsilon_{F\downarrow}}^{\epsilon_{F\uparrow}} D(E)dE = \epsilon_{F\uparrow}(N,\zeta) - \epsilon_{F\downarrow}(N,\zeta). \tag{8}$$

This condition is equivalent to

$$I\langle D(E)\rangle = 1, \tag{9}$$

where the angular brackets $\langle ...\rangle$ denote averaging over an interval of energies between $\epsilon_{F\downarrow}$ and $\epsilon_{F\uparrow}$.

Equation (6) shows that the occurrence of the Stoner instability depends sensitively on the shape of the density of states $D(E)$ in the vicinity of the Fermi energy ϵ_F for the non-magnetic state of the system. How well can this function be approximated by an analytical formula? Figure 1 shows plots of the projected on-site densities of states calculated using the density functional full-potential linearized muffin-tin orbital (FP LMTO) approach [25], and the second-level terminated recursion expansion

$$\begin{aligned} D(E) &= -\frac{1}{\pi}\Im G(E), \\ G(E) &= \cfrac{1}{\mathcal{E} + i0 - \cfrac{b_1^2}{\mathcal{E} + i0 - a_1 - \cfrac{2b_2^2}{\mathcal{E} + i0 - a_\infty + i\sqrt{4b_\infty^2 - (\mathcal{E} + i0 - a_\infty)^2}}}}. \end{aligned} \tag{10}$$

In this equation $\mathcal{E} = E - a_0$ and the first four recursion coefficients $a_0,\ b_1,\ a_1$ and b_2 are related to the *exact* moments of the LMTO density of states via [24]

$$\begin{aligned} a_0 &= \mu_1 \\ b_1^2 &= \mu_2 \\ a_1 &= \mu_3/\mu_2 \\ b_2^2 &= (\mu_4/\mu_2) - (\mu_3/\mu_2)^2 - \mu_2. \end{aligned} \tag{11}$$

The values of coefficients a_∞ and b_∞ are chosen to provide the best fit to the LMTO density of states. Figure 1 shows that the inclusion of four exact moments in the recursion expansion makes it possible to reproduce the experimentally observed [26] two-peak structure of the density of states. At the same time Figure 1 shows that in order to reproduce the correct value of $D(\epsilon_F)$ entering the Stoner criterion of ferromagnetic instability $D(\epsilon_F)I > 1$ it is necessary to include several more higher-order moments in the expansion (10). In the treatment described below we introduce a phenomenological representation of the density of states valid in the vicinity of ϵ_F, circumventing the question about the moment-based recursion approximation of the function $D(E)$.

Depending on the overall shape of the function $D(E)$, the Stoner instability (6) can give rise to either a saturated ferromagnetic configuration corresponding to a fully occupied majority spin sub-band, where the magnetic moment ζ is equal to $10-N$, or to an equilibrium unsaturated configuration corresponding to ζ satisfying equations (8)-(9). To define the equilibrium configuration we evaluate the second derivative of the total energy with respect to magnetic moment $\partial^2 E/\partial\zeta^2$. Differentiating equations (7), we find that

$$\begin{aligned} \frac{\partial^2 E_{tot}}{\partial\zeta^2} &= \epsilon_{F\uparrow} D(\epsilon_{F\uparrow}) \frac{\partial^2 \epsilon_{F\uparrow}}{\partial\zeta^2} + D(\epsilon_{F\uparrow}) \left(\frac{\partial\epsilon_{F\uparrow}}{\partial\zeta}\right)^2 + \epsilon_{F\uparrow} D'(\epsilon_{F\uparrow}) \left(\frac{\partial\epsilon_{F\uparrow}}{\partial\zeta}\right)^2 \\ &+ \epsilon_{F\downarrow} D(\epsilon_{F\downarrow}) \frac{\partial^2 \epsilon_{F\downarrow}}{\partial\zeta^2} + D(\epsilon_{F\downarrow}) \left(\frac{\partial\epsilon_{F\downarrow}}{\partial\zeta}\right)^2 + \epsilon_{F\downarrow} D'(\epsilon_{F\downarrow}) \left(\frac{\partial\epsilon_{F\downarrow}}{\partial\zeta}\right)^2 - \frac{1}{2} I \\ \frac{\partial^2 N}{\partial\zeta^2} &= D'(\epsilon_{F\uparrow}) \left(\frac{\partial\epsilon_{F\uparrow}}{\partial\zeta}\right)^2 + D(\epsilon_{F\uparrow}) \frac{\partial^2 \epsilon_{F\uparrow}}{\partial\zeta^2} + D'(\epsilon_{F\downarrow}) \left(\frac{\partial\epsilon_{F\downarrow}}{\partial\zeta}\right)^2 + D(\epsilon_{F\downarrow}) \frac{\partial^2 \epsilon_{F\downarrow}}{\partial\zeta^2} = 0 \\ \frac{\partial^2 \zeta}{\partial\zeta^2} &= D'(\epsilon_{F\uparrow}) \left(\frac{\partial\epsilon_{F\uparrow}}{\partial\zeta}\right)^2 + D(\epsilon_{F\uparrow}) \frac{\partial^2 \epsilon_{F\uparrow}}{\partial\zeta^2} - D'(\epsilon_{F\downarrow}) \left(\frac{\partial\epsilon_{F\downarrow}}{\partial\zeta}\right)^2 - D(\epsilon_{F\downarrow}) \frac{\partial^2 \epsilon_{F\downarrow}}{\partial\zeta^2} = 0. \end{aligned} \tag{12}$$

Using the last two equations, we simplify the first equation as

$$\frac{\partial^2 E_{tot}}{\partial\zeta^2} = D(\epsilon_{F\uparrow}) \left(\frac{\partial\epsilon_{F\uparrow}}{\partial\zeta}\right)^2 + D(\epsilon_{F\downarrow}) \left(\frac{\partial\epsilon_{F\downarrow}}{\partial\zeta}\right)^2 - \frac{1}{2} I. \tag{13}$$

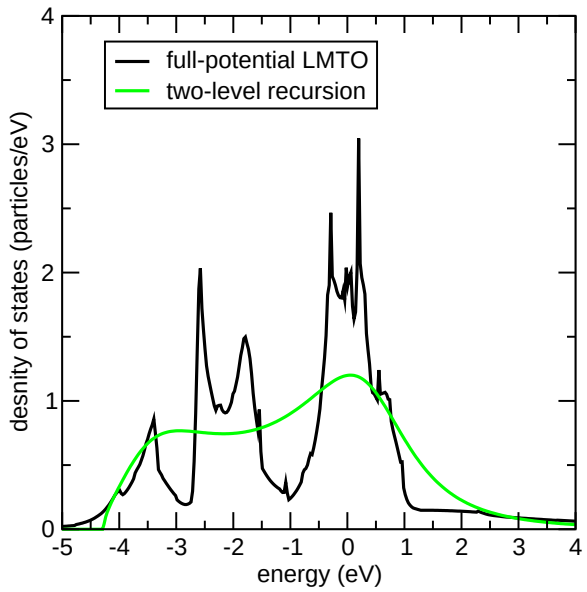

FIG. 1: Comparison of the projected on-site densities of $3d$-states of bcc iron evaluated using the density functional LMTO approach and the second-order terminated recursion expansion (10). The origin of the energy axis is chosen at the Fermi energy of the non-magnetic state ϵ_F, and the total area under the curves is normalised to the total number of electrons in a fully occupied $3d$-band $\int D(E)dE = 5$. The moments of the LMTO density of states are $\mu_1 = -0.815$ eV, $\mu_2 = 3.297$ eV^2, $\mu_3 = 2.988$ eV^3 and $\mu_4 = 43.686$ eV^4, where μ_2, μ_3 and μ_4 are defined by shifting the centre of gravity of the curve to $E = \mu_1$. The corresponding recursion coefficients are $a_0 = -0.815,\ b_1 = 1.816,\ a_1 = 0.092,\ b_2 = 3.022,\ a_\infty = 3.409,\ b_\infty = 3.841$ eV.

Taking into account the fact that at the minimum point $\partial\epsilon_{F\uparrow}/\partial\zeta = 1/2D(\epsilon_{F\uparrow})$ and $\partial\epsilon_{F\downarrow}/\partial\zeta = 1/2D(\epsilon_{F\downarrow})$, we arrive at

$$\frac{\partial^2 E_{tot}}{\partial\zeta^2}\Big|_{min} = \frac{1}{4}\left[\frac{1}{D(\epsilon_{F\uparrow})} + \frac{1}{D(\epsilon_{F\downarrow})}\right] - \frac{I}{2}. \tag{14}$$

At the minimum point the second order derivative of energy is positive $\partial^2 E_{tot}/\partial\zeta^2 > 0$ and hence, according to equation (14), the *geometric* average $\overline{D(E)}$ of the two densities of states $D(\epsilon_{F\uparrow})$ and $D(\epsilon_{F\downarrow})$,

$$\overline{D(E)} = \left\{\frac{1}{2}\left[\frac{1}{D(\epsilon_{F\uparrow})} + \frac{1}{D(\epsilon_{F\downarrow})}\right]\right\}^{-1}, \tag{15}$$

satisfies the condition $\overline{D(E)}I < 1$.

Therefore we find that the equilibrium ferromagnetic configuration is fully defined by the

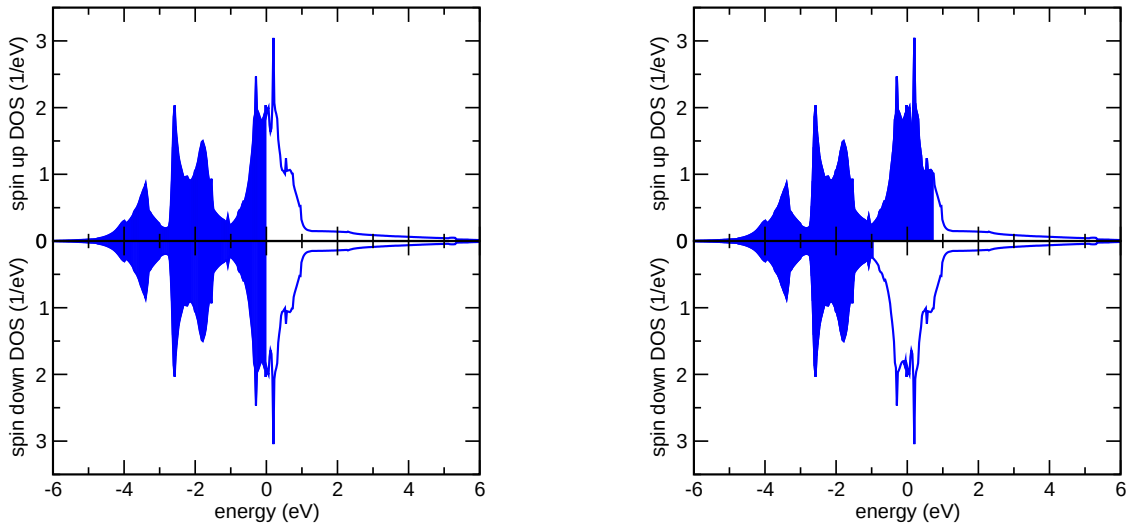

FIG. 2: Density of states plots illustrating how the spin up and spin down $3d$-bands are occupied in the non-magnetic (left) and in the ferromagnetic (right) configurations of body-centred cubic α-iron. In the non-magnetic state the density of states at the Fermi energy $\epsilon_F = 0$ is high, giving rise to the Stoner instability described by equation (6). The ferromagnetic solution shown in the right panel is stabilized once $\epsilon_{F\downarrow}$ reaches the minimum of the density of states for the minority spin band. The densities of states were evaluated using the FP LMTO method [25].

three conditions

$$\begin{aligned} D(\epsilon_F)I &> 1, \\ \frac{I}{\epsilon_{F\uparrow} - \epsilon_{F\downarrow}} \int_{\epsilon_{F\downarrow}}^{\epsilon_{F\uparrow}} D(E)dE &= 1 \\ I\left\{\frac{1}{2}\left[\frac{1}{D(\epsilon_{F\uparrow})} + \frac{1}{D(\epsilon_{F\downarrow})}\right]\right\}^{-1} &< 1. \end{aligned} \tag{16}$$

Note that while the Stoner instability condition requires that the density of states at the Fermi energy of the non-magnetic state must be high, in the equilibrium *ferromagnetic* configuration the value of $\overline{D(E)}$ is expected to be low. The last of the three conditions (16) can be satisfied if the magnitude of *either* $D(\epsilon_{F\downarrow})$ or $D(\epsilon_{F\uparrow})$ is low or, in other words, the ferromagnetic state can be stabilized by either $\epsilon_{F\uparrow}$ reaching the upper edge of the $3d$-band or by $\epsilon_{F\downarrow}$ descending into the minimum of the density of states at the centre of the band. Figure 2 shows that it is the second of the two scenarios that is realized in bcc α-iron.

Alternatively, the formation of a stable ferromagnetic configuration can be investigated by analysing the dependence of the total energy E_{tot} on the magnetic moment ζ. Figure 3

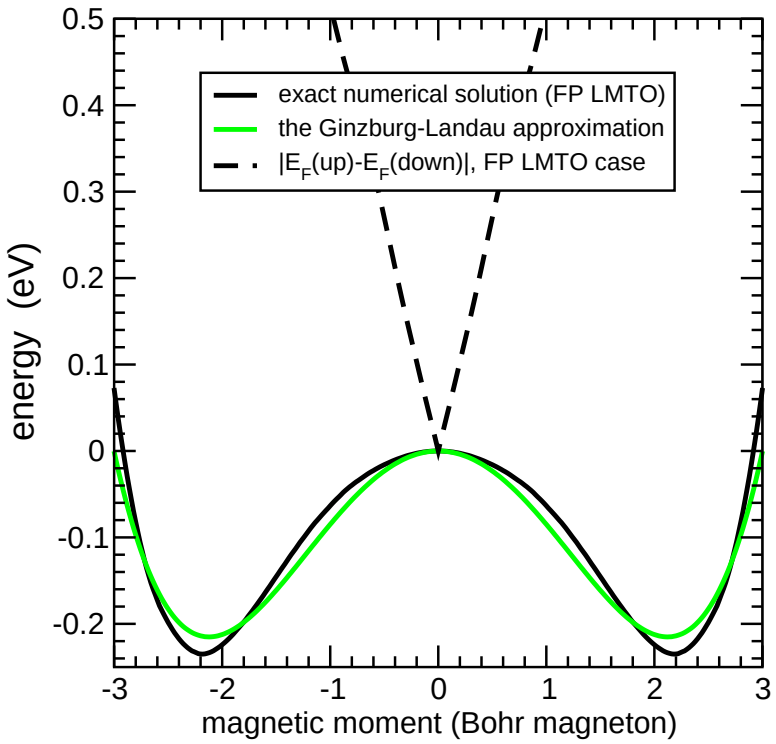

FIG. 3: The black solid line shows the magnetic part of the total energy $E_{tot}(\zeta)$ given by equation (1) calculated numerically using the FP LMTO density of states [25] and assuming that $I = 0.78$ eV and $N = 6.57$. The green solid line approximates the numerical solution by the Ginzburg-Landau model $E_{tot}(\zeta) = \alpha\zeta^2 + \beta\zeta^4$, where $\alpha = -9.55 \cdot 10^{-2}$ eV and $\beta = 1.06 \cdot 10^{-2}$ eV. The dashed curve shows the difference between the Fermi energies of spin up and spin down states plotted as a function of magnetic moment ζ.

shows that the occurrence of the symmetry-breaking Stoner instability at the point $\zeta = 0$ (corresponding to the pattern of occupation of spin-up and spin-down states shown in the left panel of Figure 2) lowers the total energy until the system reaches equilibrium at one of the two points $\zeta = \pm 2.26\mu_B$. The pattern of occupation of majority and minority spin bands corresponding to the stable ferromagnetic solution with $\zeta = +2.26\mu_B$, i.e. to the right minimum of the curve shown in Figure 3, is illustrated in the right panel of Figure 2. The other ferromagnetic solution with $\zeta = -2.26\mu_B$ corresponds to the transposed configuration of occupation numbers of minority and majority spin bands.

III. THE MAGNETIC INTERATOMIC POTENTIAL

The Stoner model of band magnetism provides a fairly accurate microscopic description of the mechanism responsible for the onset of ferromagnetism in an ordered crystalline state of α-iron. But how can this be linked to a local picture of magnetism in a deformed crystal where the local environment of every atom, its local electronic configuration, and hence its local magnetic moment vary from one site to another? The main difficulty associated with constructing a viable molecular dynamics model of magnetism consists in the fact that strain fields are described by relatively slowly varying functions of spatial coordinates and hence a meaningful simulation has to involve a large supercell containing millions of atoms. The simplicity and robustness of the model linking the electronic structure (and, hence, magnetic) aspect of the simulation with elasticity appears to be one of the most significant criteria, determining the direction in which our investigation has to proceed to address the problem.

A natural choice of approximation that we are going to use here is suggested by the shape of the curve describing the function $E_{tot}(\zeta)$ shown in Figure 3. Indeed, this characteristic double-well curve is well known in the phenomenological treatment of phase transitions, where the dependence of energy on an order parameter is given by the Ginzburg-Landau model [27]. In this model the energy is approximated by a sum of a second-order and fourth-order term

$$E_{tot}(\zeta) = E_0 + \alpha\zeta^2 + \beta\zeta^4. \tag{17}$$

By choosing $\alpha < 0$ and $\beta > 0$ we obtain a double-well energy curve where the high-symmetry non-magnetic $\zeta = 0$ configuration is unstable and where the two symmetry-broken solutions corresponding to

$$\zeta_\pm = \pm\sqrt{-\frac{\alpha}{2\beta}}, \tag{18}$$

have the same energy $E(\zeta_\pm) = E_0 - \alpha^2/4\beta$. Figure 3 shows that the curve $E_{tot}(\zeta)$ calculated numerically using the density-functional LMTO density of $3d$-states can be very accurately approximated by the Ginzburg-Landau expression (17). Furthermore, Figure 3 shows that within a sufficiently broad range of variation of magnetic moment the difference between the Fermi energies of spin-up and spin-down sub-bands varies almost linearly as a function of ζ, suggesting a possible link between equations (1) and (17).

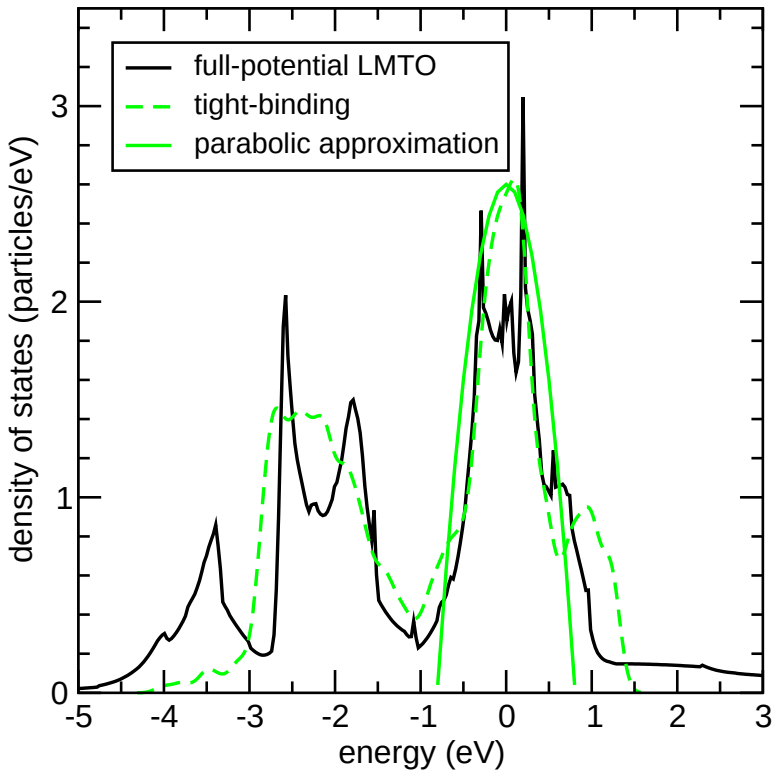

FIG. 4: Sketch illustrating the approximation in which the peak of the density of states near the Fermi energy ϵ_F is described by an inverted parabola centered at the origin. The dashed curve represents the density of states evaluated using the tight-binding approach developed in Ref. [31]. The accuracies of the tight-binding and the parabolic approximations near the origin are similar.

The derivation of the 'magnetic' atom potential involves two approximations described in Refs. [17, 28]. Firstly, we assume that the density of states has a scalable form

$$D(E) = \frac{1}{W} F\left(\frac{E}{W}\right), \tag{19}$$

where W has the meaning of the width of the $3d$-band. Furthermore, W is assumed to be proportional to an effective pairwise density function ρ of the Finnis-Sinclair [29] (or the embedded atom [30]) model.

Secondly, we approximate the peak of the density of states near the Fermi energy of the non-magnetic state by an inverted parabola as shown in Figure 4. By representing the density of states $D(E)$ in the form of a sum,

$$D(E) = \frac{1}{W} F\left(\frac{E}{W}\right) = \frac{1}{W}\left[a - b\left(\frac{E}{W}\right)^2\right] + \frac{1}{W} R\left(\frac{E}{W}\right), \tag{20}$$

of a parabolic term and a regular part, where $a > 0$ and $b > 0$ are constant factors independent of W, and $|R(0)| \ll a$, we find that in the region $I > W/a$ the expression for the total energy (1) has the *double-well* Ginzburg-Landau form [17]

$$E_{tot} = -const \cdot W + \frac{a}{4}\left(\frac{\epsilon_{F\uparrow} - \epsilon_{F\downarrow}}{W}\right)^2 (W - Ia) + \frac{b}{32}\left(\frac{\epsilon_{F\uparrow} - \epsilon_{F\downarrow}}{W}\right)^4 \left(\frac{4}{3}Ia - W\right) + \dots . \quad (21)$$

Function (21) is a maximum at the point $\epsilon_{F\uparrow} - \epsilon_{F\downarrow} = 0$ and a minimum at

$$\epsilon_{F\uparrow} - \epsilon_{F\downarrow} = \pm 2W\sqrt{\frac{a}{b}\left(\frac{Ia - W}{\frac{4}{3}Ia - W}\right)}. \quad (22)$$

Substituting (22) into equation (21) we find that the energy of the ferromagnetic configurations is given by

$$E_{tot}|_{min} = -const \cdot W - \frac{a^2}{2b}\frac{(Ia - W)^2}{\frac{4}{3}Ia - W}\Theta(Ia - W). \quad (23)$$

Here $\Theta(x)$ is the Heaviside function, $\Theta(x) = 1$ for $x > 0$ and $\Theta(x) = 0$ for $x < 0$. This has led to the following functional expression for the embedding part of the 'magnetic' many-body interatomic potential [17]

$$F[\rho] = -A\sqrt{\rho} - \frac{B}{\ln 2}\left(1 - \sqrt{\frac{\rho}{\rho_c}}\right)\ln\left(2 - \frac{\rho}{\rho_c}\right)\Theta\left(1 - \frac{\rho}{\rho_c}\right). \quad (24)$$

To fully describe an empirical model for magnetic bcc Fe suitable for molecular dynamics simulations, an energy contribution arising from a two-body repulsive potential is added to equation (24). The functional form of this pair-wise potential as well as the pair-wise density term used to determine ρ for each atom is constructed from a sum of knot functions the coefficients of which, along with the parameters A and B in equation (24), are fitted to reproduce a broad range of bulk and relaxed defect properties of magnetic and non-magnetic, bcc and fcc iron (see Ref. [17]). Within this optimisation procedure, ρ_c is set to unity thus fixing the scale of the local electronic density with respect to the critical electron density at which magnetism is completely suppressed. Parameters A and B, and the first three knot coefficients of the pair-wise repulsive potential are solved for via a linear matrix construction to exactly reproduce the bulk magnetic bcc cohesive energy, lattice constant and elastic constants. The remaining knot coefficients are chosen via a numerical optimisation procedure to reproduce as best as possible, some of the bulk properties of the magnetic fcc, and non-magnetic bcc and fcc phases, and single $\langle 100\rangle$, $\langle 110\rangle$, and $\langle 111\rangle$ dumbbell

interstitial and vacancy defect energies. During the fitting process, the reproduction of the interstitial defect energies were assigned increasing weight resulting in final defect energies to within 0.05 eV of the currently accepted *ab-initio* values [32]. In what follows simulations will employ the optimal fit referred to as case study II in Ref. [17].

The advantage of the magnetic potential model is that in practice its implementation is no different to that of the traditional embedded atom [29, 30, 33]. Despite this obvious similarity there are subtle differences between the present multi-valued formalism of the embedding energy and that of past empirical models. These differences have been described in [17]. The main fundamental difference between our treatment and the EAM model consists in the fact that our model explicitly describes *interacting* electrons while the EAM formalism is based on the tight-binding treatment of non-interacting electrons. The central development of the present work is that the functional form contained in equations (23) and (24) has an explicit theoretical grounding in itinerant band ferromagnetism, and thus can be used with a certain degree of confidence when developing a usable empirical model for ferromagnetic Fe. A prime example of this can be seen in the fitting of the interstitial dumbbell energies, where the ordering could only *easily* be achieved if the relative contributions of the magnetic and non-magnetic terms to the bulk cohesive energy where correct [17]. This indicates the fundamental importance of the magneto-elastic strain contribution to the energetics of interstitial defects — a feat not possible with an empirical model that is not physically grounded in magnetism. We conclude this section with the comment, that the numerical implementation of the magnetic potential model will continue to evolve, and that when using the first fit presented in Ref. [17] this must not be forgotten.

IV. THE MAGNETIC MOMENT OF AN ATOM

We note that (23) is derived from a minimum of the Ginzburg-Landau form with respect to $\epsilon_{F\uparrow} - \epsilon_{F\downarrow}$ (equation (21)) rather than with respect to the magnetic moment as it is stated in equation (17). In terms of the exact Stoner formalism, the choice of $\epsilon_{F\uparrow} - \epsilon_{F\downarrow}$ or the magnetic moment is equivalent since their equilibrium values are linearly related via (8). This appears not to be the case for the parabolic approximation to the density of states, in

which the magnetic moment is given by [17]

$$\zeta = \left(\frac{\epsilon_{F\uparrow} - \epsilon_{F\downarrow}}{W}\right)\left[a - \frac{b}{12}\left(\frac{\epsilon_{F\uparrow} - \epsilon_{F\downarrow}}{W}\right)^2\right]. \tag{25}$$

The situation is somewhat clarified when one considers that the range of applicability of the parabolic model to the density of states $D(E)$ is $|E| < W\sqrt{a/b}$ [17]. This is equivalent to $\epsilon_{F\uparrow} - \epsilon_{F\downarrow} < W\sqrt{a/b}$, resulting in equation (25) becoming an approximately linear relation

$$\zeta \approx a\left(\frac{\epsilon_{F\uparrow} - \epsilon_{F\downarrow}}{W}\right) = 2a\sqrt{\frac{a}{b}\left(\frac{Ia - W}{\frac{4}{3}Ia - W}\right)}, \tag{26}$$

where in the last step we have employed equation (22). Such a result reflects the fact that within a given approximation, the order parameter within the Ginzburg-Landau formalism need not formally be the magnetic moment. Indeed, in terms of the exact formalism of the Stoner model, the magnetic moment is given by (8), resulting in

$$\zeta = \left(\frac{\epsilon_{F\uparrow} - \epsilon_{F\downarrow}}{I}\right) = \frac{2W}{I}\sqrt{\frac{a}{b}\left(\frac{Ia - W}{\frac{4}{3}Ia - W}\right)}, \tag{27}$$

which for some threshold value of decreasing W (increasing volume per atom) results in a reduction of the magnetic moment with any further decrease in W. It is however in this regime where $\epsilon_{F\uparrow} - \epsilon_{F\downarrow}$ is large and W small, that $|E| < W\sqrt{a/b}$ is no longer expected to hold resulting in the entire parabolic approximation to the density of states breaking down. On the other hand, in the regime where W approaches Ia and magnetism is switched off, equation (27) approaches (26) and agreement emerges between the exact Stoner formalism and the parabolic model.

Thus there exists now the possibility to model the magnetic moment magnitude on each atom within the molecular dynamics framework at minimal additional computational cost. As with standard *ab-initio* based methods, the moment described in equations (25) and (26) is effectively a zero temperature value whose magnitude is expected to behave correctly as a function of the local strain conditions. Therefore in its present form, the magnetic potential model is unable to model ferromagnetic spin dynamics, and hence unable to describe the ferromagnetic to paramagnetic phase transition. We note however, that the Ginzburg-Landau formalism of equation (17), and generalizations to it, certainly have the possibility to do so, and therefore will be a subject of future development for the magnetic potential. Our approach also opens the way for the development of a molecular dynamics-based treatment of *directional ordering* of magnetic moments [34, 35].

With these considerations in mind, and following a similar approach of producing a usable version of (23) through (24), an approximate strategy for calculating the moment of each atom in an MD simulation would be to use the simple power law,

$$\zeta = C\left(1 - \sqrt{\frac{\rho}{\rho_c}}\right)^{\gamma}, \tag{28}$$

where C and γ are adjustable parameters chosen to reproduce the *ab-initio*-derived bulk bcc moment behaviour as a function of volume per atom.

Figure 5 shows the results of *ab-initio* calculations [36, 37] of bulk bcc magnetic moment behaviour as a function of volume per atom, and displays the expected feature that upon compression the effects of electron correlation are suppressed resulting in a reduction of the local magnetic moment. In the early work of Moruzzi *et al.* [37] compressions are considered that include the complete suppression of ferro-magnetism at a volume per atom of ≈ 7.75 Å^3. Inspection of Figure 5b in [17] reveals that for case study II, ρ approaches ρ_c at approximately 62 a.u.^{3} ($= 9.18$ Å^3), which is larger than that predicted by Moruzzi *et al.* [37]. Thus application of the simple power law expression (28) makes it impossible for case study II to accurately reproduce the moment behaviour under large compressions, and so in the present work we fit (28) to only the last five data points of Moruzzi *et al.*, which encompasses isotropic volume distortions of up to 10%. While this limits the quantitative accuracy of moment prediction of atoms in close proximity to (say) interstitial defects, the moment fields within the linear and non-linear magneto-elastic regime are expected to be well described. The optimal numerical values for the C and γ parameters are respectively 2.929 μ_B and 0.259 resulting in an equilibrium magnetic moment of 2.154 Bohr magnetons. The fact that the parabolic density of states formalism correctly predicts the moment behaviour for volume compressions that approach the complete suppression of magnetism (as seen in figure 5) offers a promising line of research for the future numerical refinement of the magnetic potential model.

V. DEFECTS IN FERROMAGNETIC IRON

In this section we describe the first molecular dynamics simulations carried out using the magnetic potential (24). Before proceeding to the simulations we point out the difference between a conventional many-body interatomic potential and the magnetic potential derived

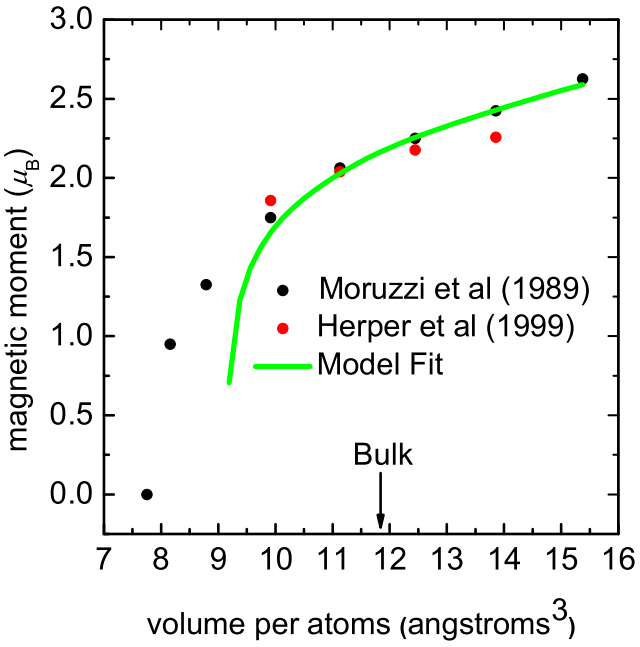

FIG. 5: Magnetic moment as a function of volume per atom under homogeneous compression.

in the previous sections. The embedding part of the magnetic potential consists of two terms, the first describing the conventional Finnis-Sinclair band part of the cohesive energy and the second representing the magnetic part of the energy. In particular, the second term represents the energy gained due to forming a symmetry-broken ferromagnetic solution corresponding to one of the two minima of the double-well curve shown in Figure 3.

The derivation given in the preceding sections makes it possible to identify the second term in (24) with the magnetic part of the total energy. Furthermore, it is also possible to relate the calculated value of the effective pairwise density function ρ on an atom to the magnetic moment associated with the atom through the use of equation (28). Hence a atomistic simulation performed using the potential (24) provides information not only about the non-magnetic and magnetic contributions to the potential energy of each atom forming a particular defect configuration, but also about the distribution of magnetic moments of atoms in the configuration. To illustrate this point, in Figure 6 we show the distribution of magnetic moments around a $\langle 111 \rangle$, a $\langle 110 \rangle$ and a $\langle 100 \rangle$ single self-interstitial atom (SIA) dumbbell defects. Among the three configurations shown in Figure 6, the $\langle 110 \rangle$ defect

has the lowest formation energy [32, 38] and the $\langle 111 \rangle$ and the $\langle 100 \rangle$ configurations are metastable. In this figure, only atoms with a local potential energy greater than -4.314 eV are shown. Those atoms with moments greater than 2.16 μ_B are coloured red and those with a moment less than 2.14 μ_B are coloured blue. We note that with these thresholds the atoms at, and very close to, the dumbbell are all shaded equally blue. Thus the significant drop in the moment that the model predicts here is not seen in this figure. As stated in the previous section, it is this regime where the model is not expected to quantitatively reproduce the moment predictions of *ab-initio* calculations, although we note that the model is able to reproduce qualitatively the correct trends found in *ab-initio* calculations. Atoms with intermediate values are coloured according to the displayed linear colour bar. In the left and central figures, the $\langle 111 \rangle$ and $\langle 110 \rangle$ dumbbell axis directions are displayed by a white line, and in the right figure, the $\langle 100 \rangle$ axis points out of the page as indicated by the white circle. These direction indicators are only approximate since the configurations are slightly off-axis to facilitate better visualisation.

Figure 6 indicates that the moment fields carried by the interstitial defects are spatially extended. In the core of the defect magnetisation is suppressed. In the regions of tensile strain around the defect magnetisation is enhanced and the magnitude of the local moments is greater than magnetic moments in perfect crystalline iron. The dominant spatial dimension of these extended moment fields is different for each defect. For the $\langle 111 \rangle$ defect it is one-dimensional, for the $\langle 110 \rangle$ defect it is two-dimensional and finally for the $\langle 100 \rangle$ configuration it is three-dimensional. These observations are supported by *ab-initio* calculations of the moment structure around relaxed interstitial defect configurations [38], although in that work only the moments of those atoms nearest to the dumbbell defect were shown.

Further evidence of the link between elastic strain and magnetism in iron is provided by large-scale simulations of dislocation loops shown in Figure 7. The perfect prismatic $\langle 111 \rangle$ loop shown in this figure was simulated using a molecular-dynamics-based conjugate gradient energy minimization routine for a supercell containing 877952 atoms. The loop itself contained 253 interstitial atoms. The orientation of the loop is idealized in the upper left hand corners of the panels where the white ovals represent the approximate orientation of the loop and the white lines represents the direction perpendicular to the loop plane. In Figure 7 only atoms with potential energy higher than -4.314 eV are shown. In the left panel these atoms are coloured according to their local magnetic moment as in Figure 6 and in the

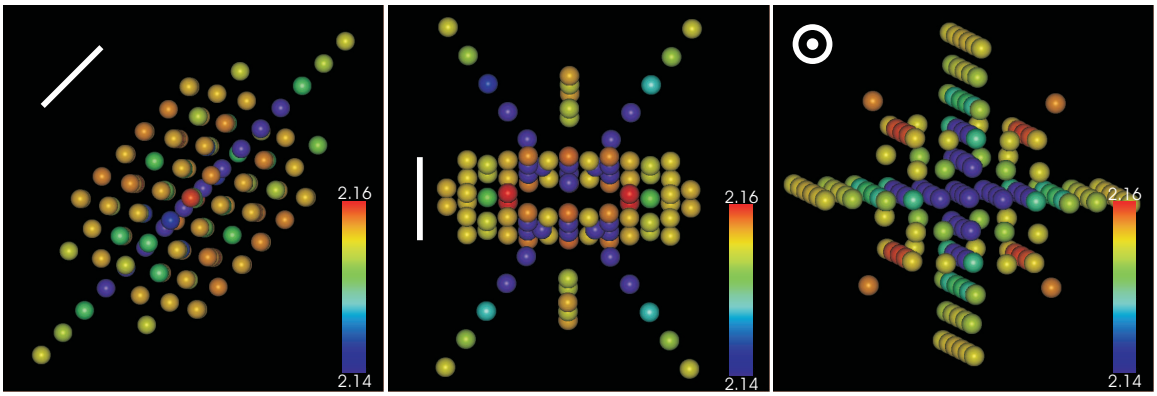

FIG. 6: Distribution of magnetic moments around a ⟨111⟩ (left) and a ⟨110⟩ (centre) and ⟨100⟩ (right) single self-interstitial atom defects. The atoms shown in the images have potential energy greater than -4.315 eV, and the colour refers to the value of magnetic moment on an atom. For the present model, the equilibrium value of magnetic moment in a perfect bcc crystal lattice is assumed to be 2.14 μ_B [37]. In the left and central panels, the ⟨111⟩ and ⟨110⟩ dumbbell axis directions are displayed by a white line. In the right panel, the ⟨100⟩ axis points out of the page as indicated by the white circle.

right panel they are coloured according to their local hydrostatic pressure calculated via the usual virial expression. The pressure colouring uses a similar scheme as that for moments, where now the upper (red) threshold in 2 GPa and the lower (blue) threshold in -2 GPa. Thus, blue represent local tensile distortions and red local compressive distortions. Figure 7 demonstrates that the distribution of magnetic moments and hydrostatic pressure are anti-correlated, i.e. magnetisation is enhanced in the regions where the hydrostatic pressure is negative, and magnetisation is suppressed where the hydrostatic pressure is high (e.g. near the centre of the loop).

One of the most significant factors determining the pathway of microstructural evolution of a material under irradiation is the thermally activated mobility of radiation-induced defects. In comparison with other body-centred cubic metals, in iron single-interstitial atom defects are relatively immobile [39]. Figure 8 shows a sequence of simulated configurations illustrating the mode of migration of a single interstitial atom defect in iron. For this figure all atoms are shown using a perspective viewing mode, where atomic colouring is via the local potential energy with respective upper and lower thresholds of -3.5 eV and -4.5 eV, and intermediate values coloured according to the indicated colour bar. In panels 1 and

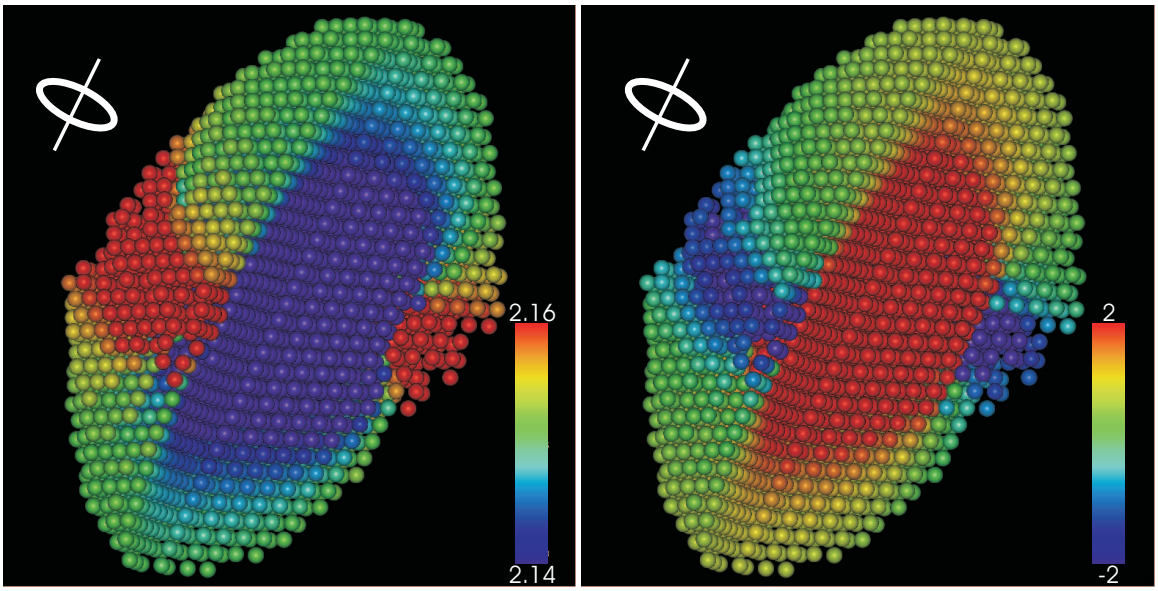

FIG. 7: Distribution of magnetic moments (left) and hydrostatic pressure (right) in the vicinity of a 253-atom ⟨111⟩ prismatic interstitial dislocation loop. The atoms shown in the images have potential energy greater than -4.315 eV, and the colour refers either to magnetic moment on an atom (left) or to local hydrostatic pressure (right). The equilibrium value of magnetic moment in a perfect bcc crystal lattice is assumed to be 2.14 μ_B. Hydrostatic pressure is given in GPa units. A segment of atoms was removed to show the distribution of magnetic moments and hydrostatic pressure in the inner regions of the dislocation loop structure.

6 the central two ⟨110⟩ dumbbell atoms can be identified as the high energy black atoms, with their ⟨110⟩ planes being identified by a trapezoid bounded by the four brown atoms. The barrier for migration is approximately 0.34 eV and the saddle point corresponds to configuration 4 shown in the left bottom corner of the figure. In agreement with *ab-initio* simulations [32], the defect migrates by performing a complex rotation around the ⟨111⟩ axis, changing its plane of orientation and thus indicating an inherently three dimensional migration mechanism. This rotation involves many atoms in the region surrounding the defect and is a collective phenomenon highlighting the quasi-particle many-body nature of the defect. Migration of single interstitial atom defects is responsible for the resistivity recovery stage I occurring in iron at approximately 120 K [39, 40].

How is this picture affected by clustering of self-interstitial atoms occurring under neutron irradiation? Molecular dynamics simulations performed using earlier versions of empirical

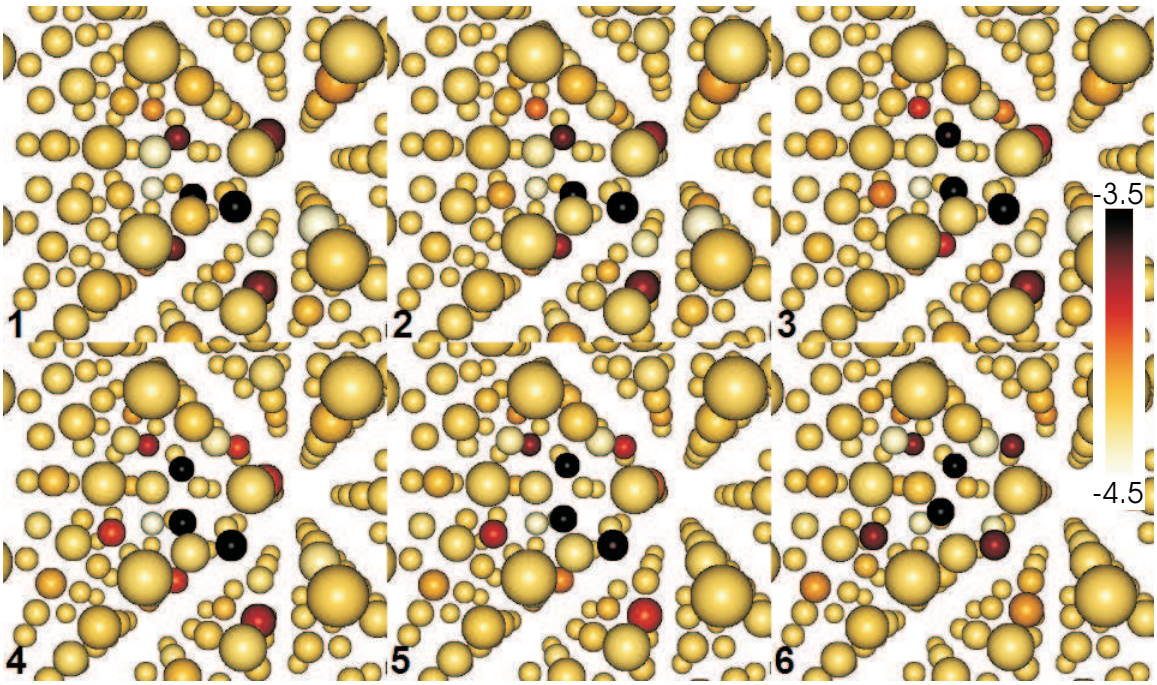

FIG. 8: A sequence of snapshots illustrating the mechanism of migration of a single self-interstitial atom defect in bcc iron. Both the initial and the final configurations of the defect have the planar ⟨110⟩-type symmetry. Colouring reflects the potential energy of each atom, given in eV units.

potentials [41] predicted that clusters of self-interstitial atoms, containing as few as two interstitial atoms, were able to diffuse one-dimensionally at very low temperatures ~ 10 K, corresponding to the activation energy of diffusion of the order of 0.025 eV (see e.g. Table 2 of Ref. [41]). On the other hand, density functional calculations by C.-C. Fu *et al.* [32] seem to suggest that clusters containing up to three self-interstitial atoms still adopt ⟨110⟩-like configurations and are characterized by a low thermally activated mobility.

To investigate this further we performed molecular dynamics simulations of the migration of self-interstitial clusters containing up to seven self-interstitial atoms. Simulations were performed at $T = 200$ K, $T = 100$ K and $T = 50$ K and extended up to 1 ns. We found that in the low temperature limit clusters containing five or fewer self-interstitial atoms eventually collapsed into the relatively immobile configurations containing ⟨110⟩-like groups of atoms. Examples of typical configurations adopted by three-, four-, five- and seven-interstitial clusters at $T = 50$ K found in our simulations are shown in Figure 9, where only atoms with potential energy exceeding by 0.1 eV the average potential energy of atoms in the lattice are shown. The symmetry of the configurations shown in the figure suggests that only

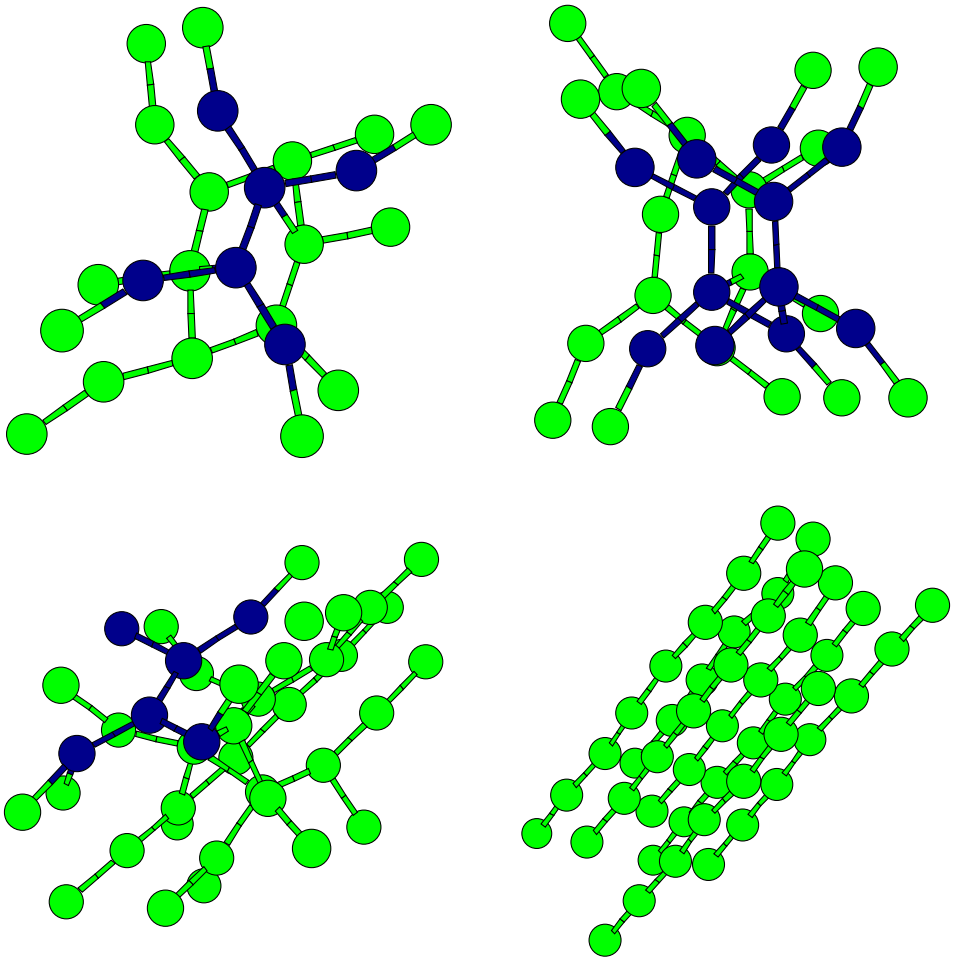

FIG. 9: Examples of three-interstitial (top left), four-interstitial (top right), five-interstitial (bottom left) and seven-interstitial (bottom right) atom defect configurations simulated using constant-temperature molecular dynamics at $T = 50$ K. Simulations were performed using supercells containing ~ 20000 atoms. The potential energy of atoms forming these structures exceeds by 0.1 eV the average potential energy of atoms in the lattice. Clusters containing fewer than five self-interstitial atoms typically adopted relatively immobile configurations where the $\langle 110 \rangle$ groups responsible for the reduced mobility of the clusters are highlighted by darker colour. The seven-interstitial atom cluster shown in the bottom right panel retained its linear $\langle 111 \rangle$ configuration at $T = 50$ K.

the seven-interstitial atom cluster retains its mobility at very low temperatures. While the onset of low temperature mobility of clusters at a certain critical size $N_c \sim 5$ warrants further systematic modelling study, here we note that this question also has direct implication for the interpretation of resistivity recovery curves of bcc iron. Indeed, clustering of self-interstitial atoms in cascades in *neutron*-irradiated iron [42] (as opposed to iron irradiated by

electrons, where clustering of interstitial atom defects probably does not occur [40]) should be expected to give rise to a fraction of defects (e.g. seven-interstitial atom clusters) exhibiting relatively high mobility at very low temperatures. This should give rise to the occurrence of new resistivity recovery stages in neutron-irradiated iron at temperatures significantly lower than 120 K. Given that the low-temperature recovery stages are well documented in the case of non-magnetic bcc metals [39], we believe that this issue should be accessible to direct experimental verification, hence providing an important insight in the microscopic origin of radiation damage in iron and ferritic materials.

Acknowledgements

We would like to thank Professor D. G. Pettifor, FRS for many inspiring and stimulating discussions. We are grateful to H. Van Swygenhoven, I. Cook and J. W. Connor for their encouragement and support of this work. Work at UKAEA was funded by the UK Engineering and Physical Sciences Research Council (EPSRC), by the EXTREMAT integrated project and by EURATOM. This work was also supported by travel grants provided to the authors by the EURATOM staff mobility programme. Several significant ideas came to us as we were commuting to or from work, and hence we would like to acknowledge the stimulating working environment provided by the First Great Western trains and by the SBB CFF FFS.

VI. APPENDIX

We write equation (1) in the form

$$E_{tot} = \int_{-\infty}^{\infty} n_{\uparrow}(E) E D(E) dE + \int_{-\infty}^{\infty} n_{\downarrow}(E) E D(E) dE - \frac{I}{4} \left(\int_{-\infty}^{\infty} n_{\uparrow}(E) D(E) dE - \int_{-\infty}^{\infty} n_{\downarrow}(E) D(E) dE \right)^2 , \tag{29}$$

where $n_{\uparrow}(E) = 1$ for $E < \epsilon_{F\uparrow}$ and $n_{\uparrow}(E) = 0$ for $E > \epsilon_{F\uparrow}$, and similarly $n_{\downarrow}(E) = 1$ for $E < \epsilon_{F\downarrow}$ and $n_{\downarrow}(E) = 0$ for $E > \epsilon_{F\downarrow}$.

By varying the occupation numbers of electronic states $n_{\uparrow}(E)$ and $n_{\downarrow}(E)$ we find the effective one-particle energies of spin-up and spin-down states

$$\frac{\delta E_{tot}}{D(E)\delta n_{\uparrow}(E)} = \epsilon_{\uparrow} = E - \frac{I}{2} \left(\int_{-\infty}^{\epsilon_{F\uparrow}} D(E) dE - \int_{-\infty}^{\epsilon_{F\downarrow}} E D(E) dE \right) = E - \frac{I}{2} \zeta$$

$$\frac{\delta E_{tot}}{D(E)\delta n_{\downarrow}(E)} = \epsilon_{\downarrow} = E + \frac{I}{2}\left(\int_{-\infty}^{\epsilon_{F\uparrow}} D(E)dE - \int_{-\infty}^{\epsilon_{F\downarrow}} ED(E)dE\right) = E + \frac{I}{2}\zeta. \qquad (30)$$

The sum of these energies

$$\begin{aligned} E' &= \int_{-\infty}^{\epsilon_{F\uparrow}} dE \left[E - \frac{I}{2}\zeta\right] D(E) + \int_{-\infty}^{\epsilon_{F\downarrow}} dE \left[E + \frac{I}{2}\zeta\right] D(E) \\ &= \int_{-\infty}^{\epsilon_{F\uparrow}} ED(E)dE + \int_{-\infty}^{\epsilon_{F\downarrow}} ED(E)dE - \frac{I}{2}\left(\int_{-\infty}^{\epsilon_{F\uparrow}} D(E)dE - \int_{-\infty}^{\epsilon_{F\downarrow}} D(E)dE\right)^2, \qquad (31) \end{aligned}$$

overestimates the magnetic Stoner term by the factor of two in comparison with the original expression (29). To compensate for the error and to return to the original expression (29) we need to add to (31) the so-called double counting correction

$$+\frac{I}{4}\left(\int_{-\infty}^{\epsilon_{F\uparrow}} D(E)dE - \int_{-\infty}^{\epsilon_{F\downarrow}} ED(E)dE\right)^2. \qquad (32)$$

This correction is by no means small, and the fact that it has to be introduced shows that in the problem of interacting electrons the meaning of the effective energies of single-particle states given by equation (30) and often used in the split-band-model treatment of magnetism, is relatively limited.

---

[1] E. P. Wigner, Phys. Rev. **46**, 1002 (1934)

[2] M. Gell-Mann and K. A. Brueckner, Phys. Rev. **106**, 364 (1957)

[3] M. Imada, A. Fujimori and Y. Tokura, Rev. Mod. Phys. **70**, 1039 (1998)

[4] J. Kübler, *Theory of Itinerant Electron Magnetism* (Oxford University Press, Oxford, 2000) chapter 4

[5] H. Hasegawa and D. G. Pettifor, 1983, Phys. Rev. Lett. **50**, 130

[6] D. G. Pettifor, Acta Materialia **51**, 5649 (2003)

[7] E. C. Stoner, Proc. Roy. Soc. London, Ser. A**169**, 339 (1939)

[8] E. P. Wohlfarth, Rev. Mod. Phys. **25**, 211 (1953)

[9] D. M. Edwards and E. P. Wohlfarth, Proc. Roy. Soc. A**303**, 127 (1968)

[10] D. G. Pettifor, Journ. Magn. Magn. Mater. **15-18**, 847 (1980)

[11] R. E. Stoller, S. J. Zinkle, J. A. Nichols and W. R. Corwin, 2004, *Workshop on Advanced Computational Materials Science: Application to Fusion and Generation IV Fission Reactors*, Oak Ridge National Laboratory Report ORNL/TM-2004/132

[12] S. L. Dudarev, Philos. Mag. **83**, 3577 (2003)

[13] D. Nguyen-Manh, A. P. Horsfield and S. L. Dudarev, Phys. Rev. B**73**, 020101(R) (2006)

[14] D. Yeşilleten, M. Nastar, T. A. Arias, A. T. Paxton, and S. Yip, Phys. Rev. Lett. **81**, 2998 (1998)

[15] E. Bonetti, L. Del Bianco, D. Fiorani, D. Rinaldi, R. Caciuffo, and A. Hernando, Phys. Rev. Lett. **83**, 2829 (1999)

[16] M.I. Mendelev, S. Han, D. J. Srolovitz, G. J. Ackland, D. Y. Sun and M. Asta, 2003, Philos. Mag. **83**, 3977

[17] S. L. Dudarev and P. M. Derlet, Journ. Phys. Cond. Matt. **17**, 7097 (2005)

[18] G. J. Ackland, Journ. Nucl. Mater. **351**, 20 (2006)

[19] L. P. Kadanoff, W. Götze, D. Hamblen *et al.*, 1967, Rev. Mod. Phys. **39**, 395

[20] W. M. Lomer, in: *Proceedings of the International School of Physics "Enrico Fermi"*, Course XXXVII, edited by W. Marshall (Academic, New York, 1967), pp. 1-21

[21] O. Gunnarsson, Journ. Phys. F: Metal Physics, **6**, 587 (1976)

[22] A. P. Sutton, *Electronic Structure of Materials* (Oxford University Press, Oxford, 1993) pp. 223-231

[23] D. G. Pettifor, *Bonding and Structure of Molecules and Solids* (Oxford University Press, Oxford, 1996) pp. 223-231

[24] D. G. Pettifor and M. Aoki, Philos. Trans. Roy. Soc. London A**334**, 439 (1991)

[25] S. Y. Savrasov, Phys. Rev. B**54**, 16470 (1996)

[26] L. Ley, O. B. Dabbousi, S. P. Kowalczyk, F. R. McFeely and D. A. Shirley, Phys. Rev. B**16**, 5372 (1977)

[27] L. D. Landau and E. M. Lifshitz, *Statistical Physics*, 3rd edition. (Pergamon Press, Oxford, 1980) pp. 446–456

[28] G. J. Ackland, M. W. Finnis and V. Vitek, *Journ. Phys. F: Metal Physics* **18**, L153 (1988)

[29] M. W. Finnis and J. E. Sinclair, Philos. Mag. **50**, 45 (1984) ; M. W. Finnis, *Interatomic Forces in Condensed Matter* (Oxford University Press, Oxford, 2003) pp. 236–237

[30] M. S. Daw and M. I. Baskes, Phys. Rev. Lett. **50**, 1285 (1983); Phys. Rev. B**29**, 6443 (1984)

[31] G. Liu, D. Nguyen-Manh, B.-G. Liu and D. G. Pettifor, 2005, Phys. Rev. B**71**, art. no. 174115

[32] C.-C. Fu, F. Willaime and P. Ordejón, 2004, Phys. Rev. Lett. **92**, art. No. 175503

[33] M. W. Finnis, *Interatomic Forces in Condensed Matter* (Oxford University Press, 2003) p. 230

[34] S. Mukherjee and R. E. Cohen, 2001, Journ. Computer-Aided Mater. Design, **8**, 107–115

[35] R. E. Cohen and S. Mukherjee, 2004, Phys. Earth Planet. Inter. **143-144**, 445–453

[36] H. C. Herper, E. Hoffmann and P. Entel, 1999, Phys. Rev. **B60**, 3839

[37] V. L. Moruzzi, P. M. Marcus and P. C. Pattnaik, Phys. Rev. B**37**, 8003 (1988)

[38] C. Domain and C. S. Becquart, 2001, Phys. Rev. B **65**, art. No. 024103

[39] *Landolt-Börstein Numerical Data and Functional Relationships in Science and Technology*, vol. 25, *Atomic Defects in Metals*, ed. H. Ullmaer (Springer-Verlag, Berlin, 1991), p. 115

[40] C.-C. Fu, J. Dalla Torre, F. Willaime, J.-L. Bocquet and A. Barbu, 2005, Nature Materials **4**, 68

[41] Yu. N. Osetsky, D. J. Bacon, A. Serra, B. N. Singh and S. I. Golubov, *Philos. Mag.* **83**, 61 (2003)

[42] C. H. Woo and B. N. Singh, *Philos. Mag.* **65**, 889 (1992)